Enhancing the performance and mechanical stability of 2D-based hybrid micro-supercapacitors using dendritic-gold as framework layer

Enhancing the Performance and Mechanical Stability of 2D-based Hybrid Micro-Supercapacitors Using Dendritic-Gold as Framework Layer

D. Arcoraci[1*], P. Zaccagnini[1,2], M. Castellino[1], A. Pedico[1], S. Bianco[1], M. Serrapede[1,2], C. F. Pirri[1,2], A. Lamberti[1,2]

[1] *Department of Applied Science and Technology, Polytechnic of Turin, Corso Duca degli Abruzzi 24, 10129, Torino, Italia*

[2] *Istituto Italiano di Tecnologia, Centre for Sustainable Future Technology, Via Livorno 60, 10144, Torino, Italia*

**corresponding author: davide_arcoraci@polito.it*

Abstract

In recent years scaling-down approaches on supercapacitors has led to the definition of Micro-Supercapacitors (μSC). The demand for these devices is increasing for many applications in microelectronics, such as wearable energy storage and self-powered sensors. Recently, many efforts have been made to achieve good results in terms of power and energy densities. However, the current research challenge is to develop a sustainable chain production, involving eco-friendly materials, such as water-based electrolytes, organic binders and low-impact active material. This work presents a hybrid μSC using low impact materials and a fully water-based solution. Different approaches were adopted for patterning the current collectors and for the deposition of the active materials. The material chosen as anode was MnO_2 deposited by electroplating, which presents pseudocapacitive behavior. The active material used for the cathode was Activated Carbon (AC), deposited by drop-casting, which works through the electric double layer (EDL) capacitance effect. The electrolyte was 1 M Na_2SO_4 in water. We investigated the addition of an interlayer micro-structure made of Dendritic-Gold (D-Gold). The results show that such a layer seems to have positive effects in terms of wettability and mechanical stability, enhancing the adhesion of the active material. Electron microscopy measurement shows the characteristic tree-like shape of the layer. The device reports a capacitance of about 14 to 23 mF cm^{-2} and a large voltage window equal to 1.6 V. The present research explores, for the first time, the effects of dendritic gold in planar electrochemical capacitors. The findings should give an important contribution for boost energy storage densities in the field of 2D micro-supercapacitors.

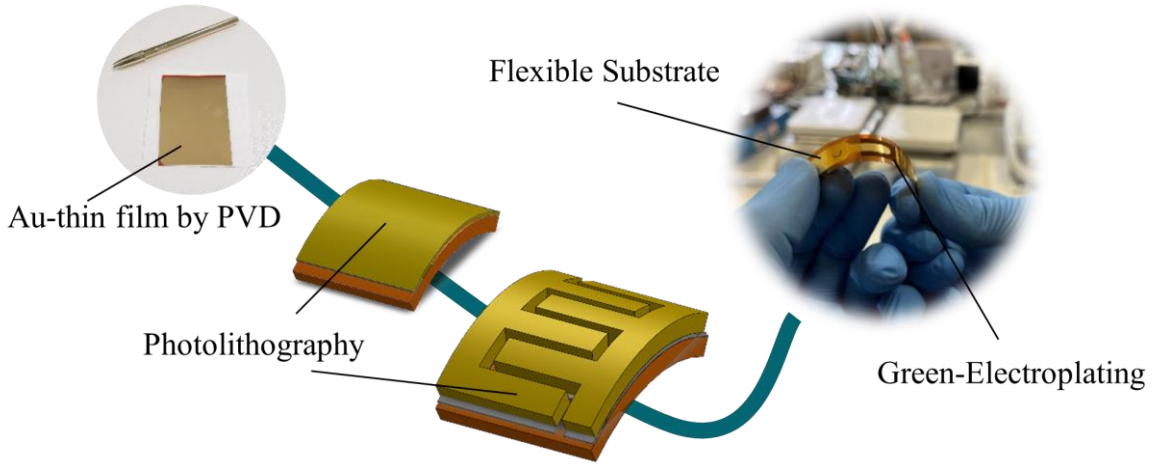

Keywords: Electrodeposition, Manganese dioxide, Planar micro-supercapacitor, Asymmetric device, MnO_2, Aqueous electrolyte, Dendritic-Gold.

1. Introduction

The miniaturization of electronics has led to the miniaturization of energy storage devices needed for the power supply or backup solutions in the Internet of Things (IoT). An example is efficient power management sensor grids, based on low-accuracy and low-power sensors/electronics. These are exploited to generate high-accuracy information thanks to data fusion employing energy harvesting solutions and energy storage systems to prolong the sensing platform life [1,2]. At present, the miniaturization trend is evolving at different scaling rates, with the integration of electronic devices developing fastest. Energy storage devices (ESDs) are currently used for portable and remote electronic systems, as well as equipped on circuit boards as power supplies or power backups. The next area to address is the reduction of power consumption of the ESDs reduction [3,4]. Currently, the flexible electronics market is growing for niche applications such as wearable and healthcare electronics. [3–8]. This growth has led to the development of ESDs compliant with mechano-chemical requirements. [9]. At present, secondary battery and capacitor technologies are exploited mainly to supply power and guarantee energy backups to electrical systems. Batteries are mostly exploited for prolonged applications because of their high energy density capabilities. Micro-batteries have been developed in the last decade, but they suffer from low power capabilities and short life cycle [10–12]. Moreover, in some cases electrolytic capacitors are used rather than batteries because power backup operations do not require prolonged functioning. Despite the high-power capabilities of electrolytic capacitors, their energy density is so low that sometimes several devices are placed in parallel to achieve the desired functionality.

Supercapacitors (SCs) can provide sufficiently high-power densities, with energy densities well above the electrolytic capacitor's performances. SCs possess also longer life cycle if compared to batteries, especially if the energy storage mechanisms are limited to the surface [13]. SCs properties and electronics power requirements led research focusing on the development of miniaturized SCs, called micro-supercapacitors (μSCs), suitable for power supply and especially as power backups. [14]. Micro-supercapacitors represent a valuable alternative to low-energy-density electrolytic capacitors. μSCs have a small footprint, relatively high energy density, and the ability to quickly discharge to provide high-power densities [15]. In this framework, the development of low environmental impact processes is of great importance due to the current energetic policies [16]. Unfortunately, for a long time, technological progress and profit prevailed over environmental concerns [17]. Herein, we present a μSC fabricated mainly via electrochemical steps in aqueous environment. The electrochemical fabrication process can be considered sustainable if the consumed electricity comes from sustainable electrical energy sources, such as solar panels. If the main source of electrical energy comes from fossil fuels, electrochemical processes and related products inherit their contribution to the environmental impact. [18] In view of the transformation toward a zero-carbon energy sector, the so-called energy transition, the development of sustainable and low-impact electrochemical processes is then of relevance to follow the sustainable development goals. μSCs potentialities are in the exploitation of these devices increasing for many applications in microelectronics, such as wearable electronics energy storage recovery and self-powered sensors. Recently, many efforts have been done to achieve good results in this field in terms of power and energy densities by using a sustainable chain production that becomes the driving force of research challenges. Moreover, particular attention was devoted to eco-friendly material, like water-based electrolytes, organic binders, and low environmental impact active materials. Boosting the energy density of μSCs is currently performed via electrode engineering. Asymmetric devices are designed to extend devices voltage window and improve electrode capacities thus increasing the overall energy density [19]. In this approach, charge balancing is a key design route. The charge balancing procedure is much adopted in conventional devices [20–25] while not so frequently reported in the field of μSCs [8,26]. In the work of Asbani et al., the charge balancing of a μSCs is carried out by properly balancing the electrode thicknesses of both vanadium nitrate and ruthenium oxide. In this report, they show how the exploitation of asymmetrical architectures allows to extend the operative voltage window (OVW) of the device up to 1.15V in 1 M KOH aqueous electrolyte. The device rated 20 μWh cm^{-2} at power

densities above 1 mW cm^{-2}, which represented an increase in the energy storage capability by a factor of 5 with respect to symmetrical configurations[27]. The procedure consists in the optimization of electrodes' capacities to guarantee the maximum polarization, thus the maximum stored energy, of the single electrodes.

In this work we present the fabrication of an aqueous-based, water-processed, hybrid μSC. Top-down and bottom-up approaches were combined to successfully realize a flexible hybrid μSC on a polyimide (PI) substrate. Bottom-up processes were carried out in water-based solution. Top-down photolithographic steps were used to pattern the current collectors. The anode material was MnO_2 deposited via electrochemical methods. The cathode material was activated carbon (AC) deposited by drop casting. All the active materials were deposited on dendritic gold current collectors allowing for improved mass loading and adhesion. According to the result, the layer seems to have positive effects in terms of wettability and mechanical stability also improving the adhesion of the active materials. The selected active materials have been exploited in the literature as electrode materials for asymmetric supercapacitors [28,29]. Both materials, AC and MnO_2, are relatively large available. Moreover, their deposition does not require, in principle, several processing steps since manganese can be electrodeposited and thermally oxidized while activated carbons can be deposited via electrophoresis. Manganese oxide is a transition metal oxide (TMO) having high theoretical capacitance of several hundreds of F/g, low-cost, natural abundance, and good environmental compatibility [30,31]. It can be electrodeposited via aqueous media as reported in the literature reducing the environmental impact of its processing [32]. Carbon materials can be deposited via electrophoresis from organic solvents [33–36] although in some works water-based processes have been reported [37]. The presented device is obtained on PI as a suitable substrate for flexible electronics. Via physical vapor deposition (PVD) processes, a chromium adhesion layer is added to allow evaporated gold adhesion to the substrate. Via lithographic steps, the μSC interdigitated electrodes are obtained. (D-Gold is then electrochemically grown [38] on both current collectors and exploited as substrates for the electrochemical deposition of manganese oxide [39] on one electrode and for the electrophoretic deposition (EPD) of activated carbons on the other electrode. The EPD process was carried out in water suspension of AC particles, in an unconventional setup, which will be fully described in the next sections. The active materials were chosen to get a high-voltage aqueous system since at neutral pH manganese oxide allows wide anodic polarization while carbon allows for wide cathodic polarization. Moreover, activated carbons are the state-of-the-art materials for electrical double layer capacitors (EDLC) production while manganese oxide is non-toxic, cheap, and widely available on earth's crust. The obtained asymmetric μSC showed a remarkable operative voltage of 1.6 V which is in the range of the current literature results [40–43]. Moreover, the rated areal capacitance was 23.0 mF cm^{-2} with an areal energy density of 5.5 μWh cm^{-2}.

2. Experimental

The fabrication of 2D interdigitated μSCs is described below. The technological process of the μSC combines a top-down approach to fabricate the 2D interdigitated current collectors and bottom-up selective deposition of MnO_2 thin films.

2.1. Current collector fabrication

The technological process, for the fabrication of electrodes, is compatible with the microfabrication methods available in the semiconductor industry. The first step was a thermal resistive Physical Vapor Deposition (PVD): the process is aimed to deposit metallic current collectors over a Kapton© substrate, using tungsten pot as hot vapor source. The Kapton© substrate was 10 cm x 10 cm and it was cleaned by sonication for 1h and treated in an oxygen plasma for 5 min prior to the deposition process. Two metal layers of chromium and gold were deposited onto the substrate, from pellets precursor with a purity of 99.8 %. Less than 10 nm of chromium were used as adhesion layer, while 100 nm gold thin film were used as metal seed layer for the subsequent phases. A deposition rate of 1.9 Å s^{-1} has been set with a level vacuum in chamber of about $5 \cdot 10^{-4}$ Pa.

2.2. Patterning

Photolithography and wet etching were used to perform the pattern (Fig. 2), the design of which consists in a single digit separation, with a distance between the electrodes of 100 μm. The single digit geometry shown in Fig. 2, was patterned onto the metal film by photolithography. In detail, photoresist AZ-1518 (Microchemicals GmbH, Germany) with a thickness of about 1200 nm was firstly deposited on the surface through spin coating technique at 4000 rpm for 45 s. Afterwards, the sample was soft baked to remove the solvent at 110 °C for 1 min. Then the sample was exposed by using UV Lamp (3 mW/cm^2) through a Mylar mask. After that, the sample was immersed in AZ400k developer solution for 35 s. Finally, the patterned interdigital Cr/Au current collector was obtained by wet etching in gold etch solution for 10 min and in chromium etch solution for 35 s

2.3. Growth of the dendritic interlayer

After photolithography, commercial Au-precursor solution (NB Semiplate Au 100 TH, MicroChemicals GmbH) was used in an electrodeposition setup in three-electrode configuration. The working electrode (WE) was connected to the interested electrode, the counter electrode (CE) was a pure gold sheet thick 50 μm and as reference Ag/AgCl electrode was used. The deposition was performed in galvanostatic mode by applying a density current between the WE and the CE of 1.4 mA/cm^2 for 450 s, while electrodes were maintained at 4 cm distance. As shown in the figure (Fig. 1c) the current density was varied to obtain a deposition rate curve to find the best mass loading parameters. The layer deposited presents a dendritic growth, which shows a characteristic tree-like shape (Fig. 3a). The form is due to the fast growth that induced particularly crystallographic orientations.

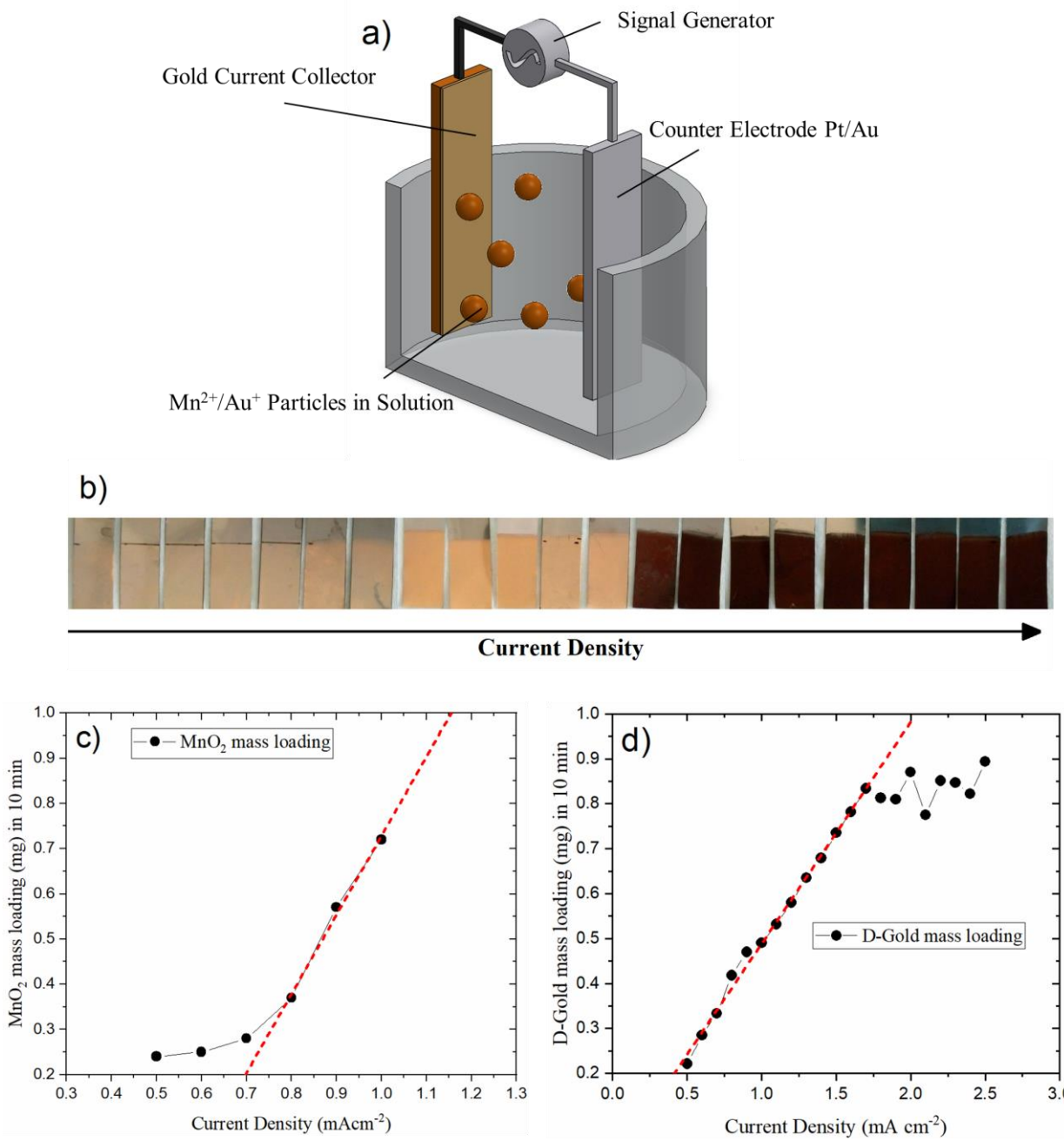

Fig. 1 (a) Schematic of the plating cell. (b) Photograph of the sample showing the deposition color gradient given by changing density current during D-Gold plating on Ti foil. (c) Mn^{2+} deposition curve changing density current during the process, using an aqueous solution of $Mn(CH_3COO)_2$ Na_2SO_4 provided by SigmaAldrich in milli-Q water. (d) D-Gold deposition curve obtained changing density current during the process. Solution used NB Semiplate Au 100 TH provided by Microchemical GmbH.

2.4. Active material deposition

For the deposition of the active materials onto the current collectors, two approaches were used. For the positive electrode, manganese dioxide was chosen as the storage material. A neutral (pH 7) plating solution of Manganese (II) Acetate 0.1 M and Sodium Sulfate 0.1 M (acting as the supporting salt) was used as precursor. Both salts were provided by SigmaAldrich, Milli-Q water was used as solvent. The setup configuration for the galvanostatic electrodeposition, was made up by three electrode parallel plates. Working electrode, connected to the interested electrode (positive one), applying a density current of 0.9 mA/cm^2 for 1000 s between working and counter electrode. Here reported the plating reaction.

$$Mn^{2+}_{(aq)} + 2e^- \rightarrow Mn_{(s)} \quad (1)$$

The distance between WE and CE was fixed to 4 cm. After plating, samples were washed in DI water and dried in an oven at 60 °C for few 48h, and mass loading was measured before and after the process with a Kern ALJ 210-5A Analytical balance with a linearity parameter of 0.1 mg. Two trials were made to define deposition rate curves: one involves Manganese, the second one Gold (Fig. 1c 1d). Moreover, different supporting salts have been involved to find the stability of the solution, such as Potassium Sulfate or Magnesium Sulfate, even if, no relevant improvements were observed. After plating of MnO_2 a calcination process was applied, with the sequent temperature profile: 1 h at 60 °C, 4 h at 300 °C and 1 h at 60 °C h, in Buchi Glass Oven (no vacuum) [44].

The active material for the negative electrode was deposited through drop casting technique. A water-based colloidal solution 0.9 %wt of AC Kuraray was used with a very low amount of water binder 0.03 %wt. 100 µl of solution was cast onto the surface [15]. An electric field, generated by a DC voltage of about 50 Vcm^{-1}, was applied between the electrode cast and a needle. The positive potential was imposed on the substrate electrode, the negative on the needle immersed in the meniscus. The strong electric field starts to an electrophoretic process, that enhances the contact of the carbon particles on the surface of the current collector (zeta potential measurements were made to explore the polarization shell of the activated carbon, it results a zeta potential of about -30mV in DI water). Both positive and negative electrodes were analyzed separately in tree electrodes configuration to obtain for each electrode the charge storage performance. Two different electrodes were prepared one with thermal treatment and one without thermal treatment for XPS measurement, (Fig. 4a) to understand the oxidation state of the active material surface before and after the thermal process [45]. After this preliminary analysis a planar hybrid device was built. Although referring to a bulk configuration, the first innovative study, on the concept of hybrid capacitor, was originally proposed by Hong [46] and successively by T. Brousse et al. [47]. The studies propose an asymmetrical configuration, involving activated carbon and manganese oxide in aqueous media, in order to enlarge the operating voltage window and give higher energy density. With the same intention, the study proposed here aims at obtaining energy enhancement on planar devices.

2.5. Packaging

The planar hybrid single interdigit device, was sealed in a pouch cell package in a low vacuum chamber to prevent electrolyte drying. A glass fiber Whatman separator of grade D exfoliated to 300 µm thickness in order to keep the volume device low, was used to retain the electrolyte. The separator soaked with 220 µL of Na_2SO_4 1 M, was used to simplify the welding step. A thermoplastic foil, through the in/out edge, was posed to obtain a good isolation of the external contact point.

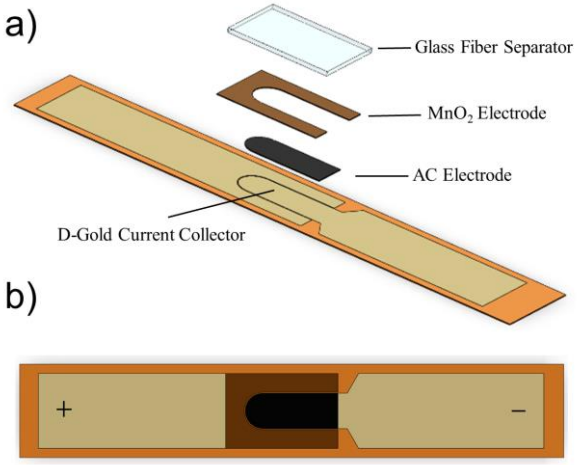

Fig. 2 (a) illustration of the single interdigit device. (b) Top view of the device

2.6. Characterization techniques

XRD patterns of the electrodeposited manganese oxides were collected on a powder x-ray diffractometer (Empyrean, Anton Paar, STATE) with CuKα radiation (λ = 1.54052 Å) at 40 kV, and 30 mA, and a 0.013 step size of 2θ angle from 10 to 100. The samples were placed onto a zero-background stage holder to avoid further signals. The software QualX with RRUFF- and COD-database were used for the phase identifications. MAUD free software was employed for the quantitative phase analysis and the refinement. Fityk free software was employed for the deconvolution of the peaks and used only for graphical purposes. For the Reitveld refinement The Crystallographic Open Database (COD) was used, the COD numbers employed are 00-900-8518, 00-210-5394, 00-900-9111, 00-900-8463, 00-900-1963, 00-151-0524. **XPS** (X-ray Photoelectron Spectroscopy) analyses have been carried out by means of a PHI 5000 Versaprobe (Physical Electronics, Chanhassen, MN, USA) spectrometer, equipped with an Al k-alpha monochromatic source (1486.6 eV). During the measurements samples have been subjected to a combined electron and Ar ion gun neutralizer system, to decrease the electrical charging effect induced by photoelectrons extraction. The semi-quantitative atomic concentration and fitting procedures were acquired using Multipak 9.7.0.1 Version dedicated software. All core-level peak energies were referenced to C1s peak at 284.8 eV (due to adventitious carbon) and the background contribution in high-resolution (HR) scans was subtracted by means of a Shirley function.

Micro-Raman spectroscopy was performed by using a Renishaw InVia Qontor Raman microscope. A laser diode source (λ=532 nm) was used with 5 mW power, and sample inspection occurred through a microscope objective (50X), with a backscattering light collection setup. The Raman spectrum analysis was carried out with Fityk software [48]. Lorentzian functions were used as fitting functions. All the data are reported with baseline correction.

The electrochemical synthesis and **electrochemical** characterizations of the single electrodes were firstly performed for each single electrode by using a potentiostat/galvanostat Metrohm Autolab. The electrodes were immersed in a beaker containing the electrolyte in three electrodes cell configuration, with a platinum rod as counter electrode and Ag/AgCl as reference. OCP and subsequentially Poteziostatic Electrochemical Impedance Spectroscopy (PEIS) were performed (frequency range: 1 MHz to 10 mHz with a signal amplitude = ± 10 mV) to evaluate the electrode equivalent series resistance. Arbin BT2000 potentiostat/galvanostat was used to perform the electrochemical characterizations in the 2-electrode device. For 2D interdigitated micro-Supercapacitors, 220 μL of 1 M Na_2SO_4 aqueous electrolyte were infiltrated in the glass fiber separator.

2.7. Evaluation Formulas

The capacitance of the single electrode (C) and specific capacitance (C_m, C_A) can be estimated by CV curves using the following equations:

$$C = \frac{1}{V_w} \cdot \int I_d dt \tag{2}$$

where the integral represents the total charge passed during the discharging profile, and V_w is the potential window. The specific capacitance reported (in F/g) was calculated by:

$$C_m = \frac{1}{m_a \cdot V_w} \cdot \int I_d dt \tag{3}$$

considering only the mass of active material, the contribute of current collectors, separator and packaging is not included. Only the discharging part was taken in account. The capacitance per unit area was calculated by the following:

$$C_A = \frac{1}{A_g \cdot V_w} \cdot \int I_d dt \tag{4}$$

the area taken is the geometrical area of the entire active area, in other terms the part exposed to the electrolyte, the gap between the electrodes is included. The energy and power performance of the device were calculated using the following formulas:

$$P_d = \frac{1}{A_g \cdot t_d} \int V_d I_d dt \tag{5}$$

$$E_d = \frac{1}{A_g} \int V_d I_d dt \tag{6}$$

The surface areal factor was calculated by the following:

$$A_{real} = \frac{Q_{red}}{\Gamma} = \frac{Q_{red}}{e \cdot d_m} \tag{7}$$

Where the Q_{red} is the cumulative charge involved in the reduction peak, e is the electron charge 1.6 e^{-19} C, Γ is the charge per surface area for a gold oxide layer 384 μC cm^{-2} and d_m is surface metal atom density.

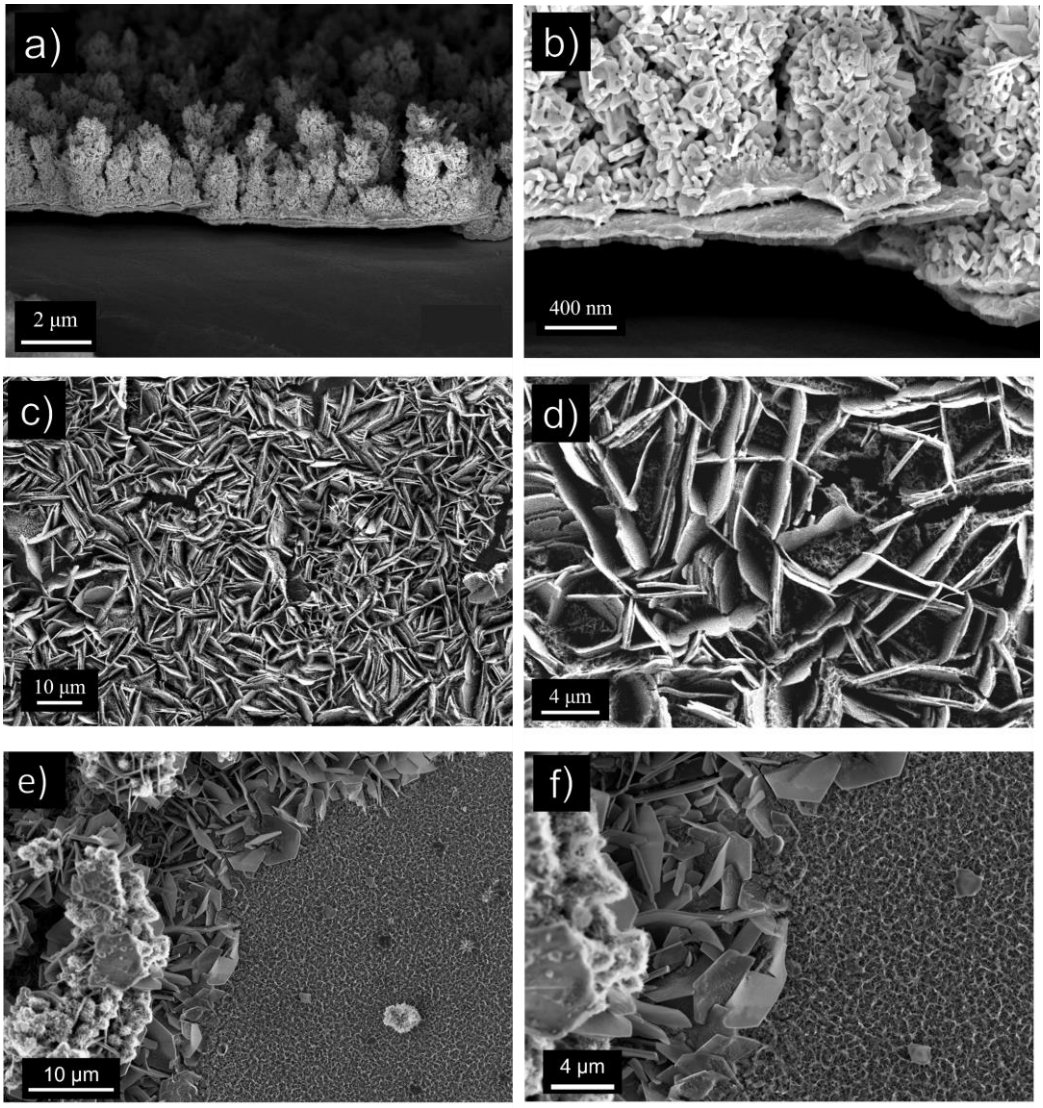

Fig. 3 (a, b)FESEM image for grown D-Gold on thif film gold. (c, d) FESEM image for grown MnO_2 on thin film gold current collector. (e, f)FESEM images with different magnification of grown MnO_2 on D-Gold current collector.

3. Result and discussion

3.1. Electrical characterization

Vander paw method, [49] was applied on the square metal film obtained through the technique. Tens of measurements have been performed resulting in a sheet resistance of the metal film of about 300mΩsquare.

3.2. Physical and Chemical Characterization

Fig. 3 shows a tilted FESEM image of a selectively grown layer of D-Gold and MnO_2. The thickness of the deposited layer was determined using SEM and confocal microscopy. The morphological and elemental analysis of the electrodes surface were performed using a Zeiss field emission scanning electron microscope (SEM). The surface chemical composition of electrodes was estimated via XPS analysis to evaluate surface chemical composition and manganese oxidation states of the deposited materials. From survey spectra (not reported), for thermal treated and as-prepared samples, we can confirm the presence of Mn, together with O, C and, in some cases, Au traces (< 1 at.%) coming from the substrate, and remnants due to precursors and solvents used during the deposition procedures (i.e. Na, K, S). We all know that Mn represents a tricky element to be fully understand by XPS technique. This is mainly due to its six oxidation states, together with the presence of multiplet splitting (for oxidation states II, III IV and VI) overlapping, and broadening due to the simultaneous presence of more than one oxidation state at the same time. For this reason, we cannot rely only on Mn 2p doublet analysis, to clearly determine Mn oxidation states. We should also consider Mn 3s doublet, from which, by checking the two peaks relative separation distance in the binding energy scale, we can obtain a further piece to complete the intricated puzzle. From Fig. 4a, we can clearly see that the two Mn 2p signals, for the thermally treated (red line) and the as-prepared (blue line) samples, are clearly different. A relative distance of 0.6 eV can be inferred between the two Mn $2p_{3/2}$ peaks together with the presence of a satellite structure (5.2 eV apart from Mn $2p_{3/2}$ maximum), for the as-prepared sample, above 644.0 eV, which is commonly attributed to shake-up losses due to MnO phase [50]. If we now consider the Mn 3s doublet (not reported) we obtain two different values for the relative distances (ΔE) between the two doublet peaks: 5.23 eV and 5.65 eV for the thermally treated and the as-prepared one. The values are in good agreement with the table proposed by Chigane and Ishikawa in [51] and is a further confirmation of the conversion of MnO into Mn_2O_3 by the thermal treatment. There are many attributions in the literature to these values [52,53], according to the oxidation state and relative crystallographic phases; but if we use the formula reported in [54] to obtain the *Average Oxidation State* (AOS) by: $AOS = 8.95 – 1.13\ \Delta E$, we can evaluate which is the main oxidation state present in the upper surface of our samples. The two calculated values are: 3.04 and 2.56 for the thermally treated and the as-prepared respectively. This means that the active material which has undergone a thermal treatment presents a mean oxidation state equal to Mn(+3) as in Mn_2O_3 or MnOOH, while the as-prepared electrode shows an oxidation state which is a mix between Mn(+3) and Mn(+2).

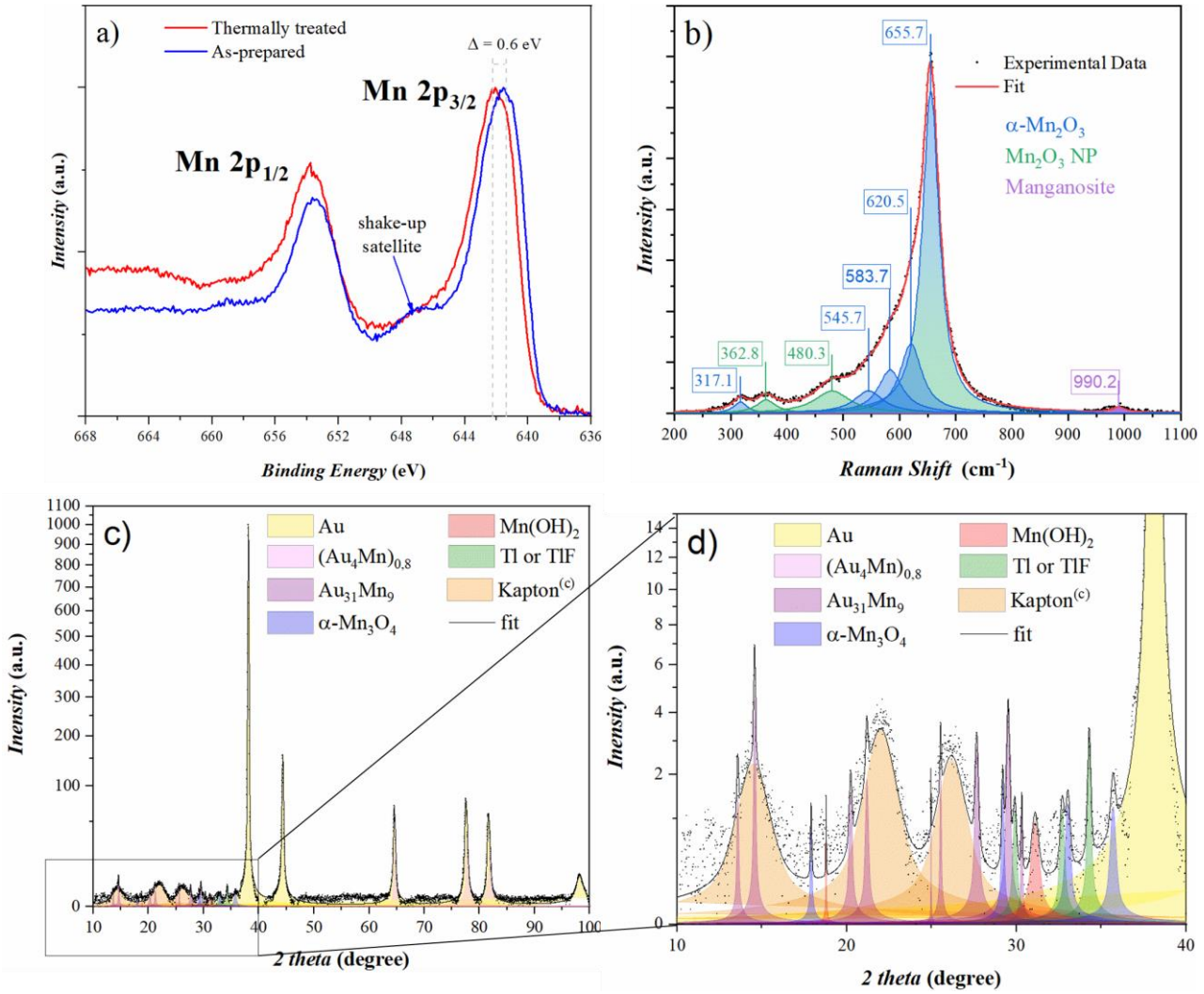

Fig. 4 (a) XPS Mn 2p doublet HR spectra for the thermally treated (red line) and as-prepared (blue line) samples (b) whole XRD pattern of the dendritic electrode after background (polynomial6) subtraction and (d) magnification for angles below 40°.

The presence of the shake-up satellite due to MnO structure already predicted the existence of a Mn(+2) component. Moreover, if we recall the relative distance highlighted in Fig. 4a between the two Mn $2p_{3/2}$ components (Δ = 0.6 eV), we can find out the same relative distance between MnO and Mn_2O_3 or MnOOH reported in M. Biesinger et al. detailed work on transition metal oxides [50].
The Raman spectrum of manganese oxides has three main regions: 200-450 cm^{-1} it is possible to find the skeletal vibrations, 450-550 cm^{-1} there are the deformation modes of the Mn-O-Mn structures and in the region 550-750 cm^{-1} the Mn-O stretching. Generally, literature reports are different among natural and synthetic samples of claimed phase. In the work of Xin et al., complete chemical physical characterization of synthesized manganese oxides/hydroxides were carried on, the abovementioned work was taken a reference for the Raman spectrums [55]. The employed laser was 532 nm continuous green light. Powders were compressed and analyzed over a glass substrate. The Raman shift scale was calibrated with a crystalline Si-wafer. The structure of manganese oxides contains the same MnO_6 octahedral building blocks, sharing edges and corners in different schemes. Such octahedral structure possesses six normal vibrational modes: ν_1, ν_2, ν_3, ν_4, ν_5, ν_6. Among these six modes, only three are Raman active ν_1, ν_2 and ν_5 whereas ν_3 and ν_4 are IR active. However, the nominally inactive modes may become active when the octahedra form layered and/or tunnel structures. Our sample showed an intense peak at 655.7 cm^{-1} which is attributed to the ν_1 vibrational mode of Mn^{3+}, with two shoulders at 620.5 cm^{-1} and 583.7 cm^{-1} still attributed to ν_1 vibrational mode of Mn^{3+} with less intensity. According to the data reported in [55], the possible phase is α-Mn_2O_3. The same peaked response of a Mn_2O_3 sample synthesized by wet chemical route only was found in different literature works [56–58]. It is worth mentioning that the same peak is a feature of Mn_3O_4

phases, as reported in other literature reports [59] as well as in [55]. However, this manganese oxide phase was not considered because of the oxidation state of manganese. The information goes in good agreement with the XPS results. Following this information, since the peak of the ν_3 mode at 703 cm^{-1} is absent, we can claim the material is not a layered or tunnel structure. Moreover, the ν_5 peak at 318 cm^{-1} is present for our sample at 317.1 cm^{-1} with not so intense activity of the skeletal modes. The ν_2 mode was found in position 545.7 cm^{-1} instead of 538 cm^{-1} as can be qualitatively appreciated also from the report of Ram et. al.[60]. Our spectrum presented two more relatively intense peaks in the range 300 to 500 cm^{-1}. According to the report of Karuppaiah et. al. [33], the two peaks can be attributed to the presence of Mn_2O_3 nanoparticles as they reported peaks at 368 cm^{-1}, 483 cm^{-1} and 652 cm^{-1}. However, particles dimensions are not clear out of this report, although precipitate powders were claimed to be handled, suggesting nanometric sizes below 100 nm. Further, in the work of Yousefi and coworkers [61]. According to the systematic study of Bernardini et. al., the small peak at 990.2 cm^{-1} can be attributed to the Manganosite phase (MnO), which is not so present since the relatively low peak intensity [44]. The usual poor crystallinity of electrolytic manganese oxides, the size of the crystallites typically limited to the nanoscale and the presence of multiple phases, make the identification and characterization of such family of compounds a real challenge with the XRD for which IR, Raman and XPS spectroscopies are more sensitive. For this reason, together with the studied electrode, two other measurements were carried out on samples prepared *ad hoc* to unravel some features of the complex pattern of the dendritic electrode itself.

The reflections at the dendritic electrode are characterized by the presence of very strong and sharp peaks imposed by the dendritic gold and by weak, but very broad, reflections arising from the Kapton© flexible substrate (evidenced in Fig. 4c XRD with the patterned yellow and orange peaks, respectively) onto which the reflections of the manganese oxides are superimposed. It is worth mentioning here that the reflections of the Kapton© support are identical before/after the thermal treatment and that in the qualitative identification and quantitative analysis they were subtracted together with the polynomial background. In order to have a less intense signal generated by the gold, the electrochemical deposition of the manganese oxide was carried out also onto a flat-smooth gold current collector with higher manganese-compounds mass loading. This sample allowed to better focus the attention to the metal oxide electrodeposited rather than to the current collector. The same sample was then annealed according to the usual procedure to prepare the dendritic electrodes. From these three measurements it was possible to follow up the evolution of the gold current collector and that of the manganese-related phases under thermal treatment. By combining a qualitative, quantitative and Rietveld refinement analysis it is possible to conclude that the flat current collector belongs to the gold Fm-3m space group with a face-centered cubic unit cell with cell parameter a = 4,099 Å that decreases to 4,080 Å after the thermal annealing. On the contrary, the average crystal size increased from 758 to 833 Å and the microstrain of the structure relaxed form 1.31μ to 1.20μ. The dendritic gold instead shows a unit cell with a = 4.076 Å and average crystal dimension much larger, above 1150 Å with microstrain of 1,35μ even after the thermal treatment. Interestingly, in the dendritic electrode, metallic gold (22 % of the weight of the sample) is not the only metallic phase. Two Au-Mn alloys were computed to be present in relevant quantity during the refinement that are $(Au_4Mn)_{0.8}$ and $Au_{31}Mn_9$, accounting the 4.45 and 1.8 % of the total weight of the sample. Regarding the manganese-based active material, onto the flat and dendritic current collectors two manganese oxyhydroxide were identified that are the Hausmannite, α-Mn_3O_4, and Pyrochroite, $Mn(OH)_2$. The latter disappeared completely after the thermal treatment on the flat gold, but a little residue remains onto the dendritic current collector (0.2 %). It is worth mentioning that before the thermal treatment the Pyrochroite had small average crystal size of about 110 Å, while the α-Mn_3O_4 showed large crystal size of 1075 Å that decreased massively to 164 Å post the annealing. By the human eye, this change in the crystalline size without altering other structural parameter of the phase, appears as a colour change from light orange to deep brown. In order to perfectly close the Reitveld refinement of the dendritic electrode, still one phase was missed (0.1 % by weight) and it is equally possible to be the metallic Tl or TlF coming as impurity from the gold electroplating solution in which a Tl-based salt

is present as brightening agent. It is possible that the residual $Mn(OH)_2$ and the Tl-based compound have been trapped in close porosities during the electrodeposition process onto such random shape or because of insufficient annealing time/temperature. All the refined parameters of the phases identified in the three samples are presented in Table XRD in the supporting information. In wet synthesis of MnO_x nanostructures, the nonequilibrium nature of crystallization at ambient temperatures initiates the competition between different metastable phases, and multivalence mixtures of manganese oxides are usually obtained [62]. Pyrochroite is in nature an abundant mineral in aquatic and wet environments which readily transforms to higher oxidation states [63] with fast kinetic. Hausmanite instead is the most stable phase of manganese oxides with the highest average oxidation state of Mn as +2.66. α-Mn_3O_4 correspond to the space group of I41/ and it has a usual spinel structure presented by the formula, $Mn^{2+}(Mn^{3+})_2O_4$ in which the Mn^{2+} and Mn^{3+} ions occupy the tetrahedral and octahedral sites, respectively, with tetragonal distortion of Mn^{3+} ions due to Jahn−Teller effect [64]. Bibyxite is a trivalent oxide, α-Mn_2O_3, ant it has a cubic structure with a space group of Ia3. In the past few decades, it has attained a significant scientific interest because of its outstanding structural architecture for supercapacitors. Chen et al. [65] proposed the phase change from precipitated wires of $Mn(OH)_2$ and their phase transformation first to α-Mn_3O_4 and then to α-Mn_2O_3 by means of thermal treatments in air or in nitrogen atmosphere. Similarly, Ramirez et al. [60] observed that when the amorphous MnO_x was heated above 450 °C (1) under air flux it turned to α-Mn_2O_3 crystal structure similar to a distorted Bibyxite and (2) under Nitrogen it crystallized into the α-Mn_3O_4 crystal structure as Hausmanite. These reactions were carried out under flowing gasses in order to feed the surface with the reactants. During the annealing procedure at 300 °C of the dendritic electrodes, instead, the atmosphere was static, therefore the oxidizing agent at the surface was probably not sufficient to feed the reaction more in depth and promote the oxidation of the Hausmanite into Bibyxite like on the electrode surface. Additionally, for those metal oxides whose families have many oxidation states, the phases on the surface are very different from those in the bulk. Song et al. [66] employed both laboratory and synchrotron-based light analysis to unravel the phases at different depth in their samples by using small angles and quartz capillary transmission XRD and they evidence the co-presence of α-Mn_3O_4 and α-Mn_2O_3 at different depth and annealing conditions. Therefore, in the present study, the evidence of an evolution of the oxidation state from the bulk through XRD (depth of analysis > 2000 nm) to the surface by Raman (<1000 nm) up to the interface by XPS (<10 nm) is presented together with the structural evolution of the current collector from flat to dendritic gold.

3.3. Electrochemical Characterization

3.3.1. Flat Gold vs Dendritic Gold Analysis

A dendrite is a crystal with a tree-like branching structure (Fig. 3a), this type of shape can be observed in different science fields, such as biology, metallurgy and crystallography. A well-known example, present in nature of these structures, are crystals formed in snowflakes. In this context, we are interested in metallic dendrites formed during electroplating deposition, and we give information about the areal surface boost obtained by covering this type of surface with active materials for supercapacitor applications. Highly porous metallic current collectors were prepared using the plating solution proposed in the experimental section. An advantage of this technique is its cleanliness, simplicity, making this easily transferable to production line with microelectronic facilities. For the characterization of the dendritic metallic layer, preliminary cyclic voltammetry in H_2SO_4 0.5 M was made. In Fig. 5a well known voltammograms of two different gold current collectors are shown: the red curve represents flat gold (F-Gold), the gray one D-Gold. Here it is possible to distinguish two regions: the oxygen one and the double-layer one. The oxygen region starts sweeping the CV over a potential above 0.9 V vs Ag/AgCl for the D-Gold electrode, and starts sweeping the CV over a potential above 1 V vs Ag/AgCl for the F-Gold electrode. We consider only the formation of thin

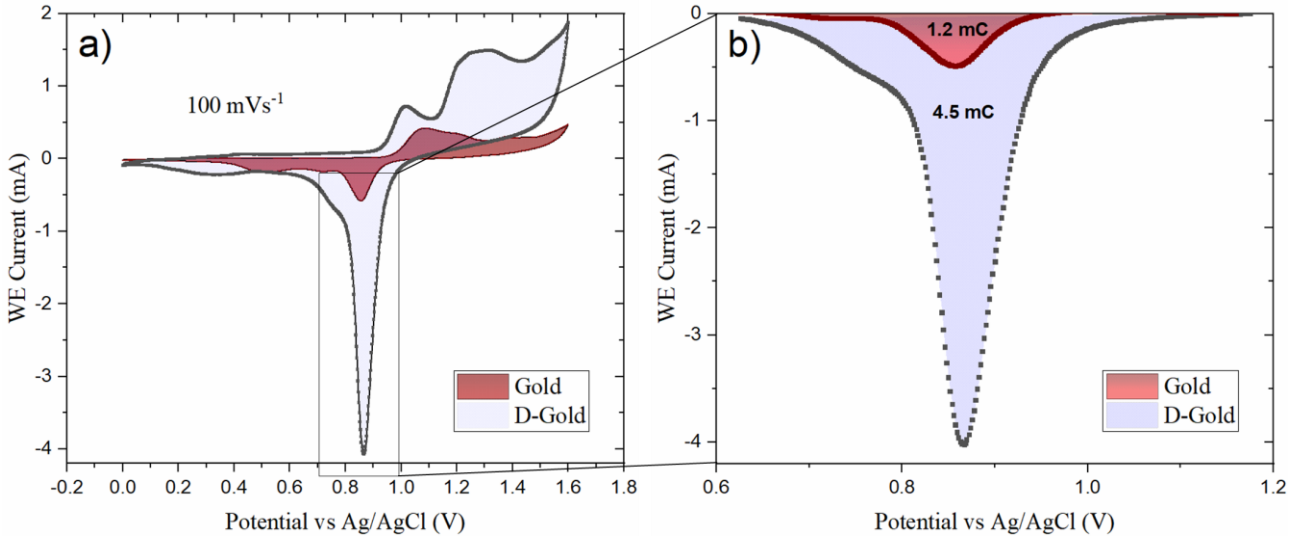

Fig. 5 show (a) CV of thinf film gold and D-Gold overlapped at 100 mVs^{-1}in H_2SO_4 0.5 M, the electrode potential is referenced to Silver/SilverCloride reference electrode. (b) Dettail of the reduction peak used for the calculation of the areal factor.

anodic oxide films through a simplified reaction during the positive sweep prior to O_2 evolution. Hence, hydrated Au oxide monolayer is formed on the electrode, this region will be involved for the evaluation of the real surface area. In the left part of the voltammograms, from 0 to 0.7 V, is evident the double-layer region where only capacitive processes take place. The evaluation of the electrochemical surface area (ECSA) was performed by estimating the reduction charge of the gold oxide at 0.87 V vs Ag/AgCl as shown in Fig. 5b. The intensity of this current peak at this reaction potential is proportional to the ECSA of the electrode. One peak refers to the flat gold in red color (Fig. 5b), and the second one, in gray, refers to the dendritic gold. The charge associated with the reduction of the oxide formed on the surface of the Au electrodes was measured to 1.2mC for flat gold and 4.5 mC for the D-Gold electrode. The quantity that we want to evaluate from this amount of charge is the ECSA and the roughness factor, i.e. the ratio between the effective area and the geometrical footprint area [67],[68]. Through eq. 7, it was obtained, from the F-Gold electrode, with a geometrical area of 0.5 cm^2, a roughness factor of about 6.6 and an ECSA of about 3 cm^2, and from the D-Gold electrode, with a geometrical area of about 0.54 cm^2, a roughness factor of about 22, and a ECSA of about 12 cm^2. The areal gain factor from thin film gold to dendritic gold is of about 4x. In terms of areal capacitance dendritic gold layer offers a specific capacitance of about 0.5 mF cm^{-2},this value was calculated through CV in Na_2SO_4 1 M in a potential window 0 to 1 V, using e. 4, reporting the absolute capacitance on to the foot print area. Further analyses were made tuning the D-Gold mass loading with respect to the active material.

3.3.2. Electrodes Analysis

The charge storage properties of the MnO_2 film onto F-Gold current collector, prepared as described in the experimental section, were first investigated through CV measurements. Furthermore, it was studied how capacitance performances change in function of the pseudo-capacitive material mass loading. Fig. 6a shows typical cyclic voltammograms obtained at a scan rate of 10mVs^{-1} between 0.1 and 1.1 V vs Ag/AgCl. The shape of the CV is almost nonlinear boxed and presents a good pseudocapacitive behavior. In Fig. 6b the performance of this electrode, changing the MnO_2 mass loading, is reported. It can be noted that the trend of the gravimetric capacitance results are linearly degressive. This experimental evidence confirms that only the Manganese atoms, a constituent of the electrode surface, are involved in the charge storage mechanism. The red line, indicating the areal capacitance, reaches a plateau of about 35 mF cm^{-2} for the electrodes with a MnO_2 mass loading over 0.25 mg cm^{-2}. In conclusion, there are no consistent advantages in raising the mass loading of manganese over 0.25 mg cm^{-2} if the final applications are planar μSCs. However, rapid degradation was observed with the F-Gold electrode from 0 to 1.1 V compared to Ag/AgCl. The wide potential window leads to delamination of the electrode and consequently to its premature damage. It is

assumed that the origin of this is due to the surface stress phenomena after a high number of cycles, which occur in the vicinity of the O_2 gas evolution region. For this reason, a limited operating potential window of 0 to 0.7 V vs Ag/AgCl was chosen to ensure long-term cycle stability. For what concern the subsequent analyses with D-Gold treated electrode, a fixed amount of MnO_2 of 0.7 mg cm^{-2} was used for three electrodes tests. The three electrodes were prepared with a mass loading of D-Gold respectively of 0.88, 1.56, and 3.34 mg cm^{-2}. The fixed MnO_2 mass loading was chosen to give more evidence to the benefit obtained involving D-Gold layer. It is immediately clear that there is difference in the shape of CV curves in Fig. 6c compared to Fig. 6a. The CV in Fig. 6c is more boxed and larger in terms of current, than the one in Fig. 6a. It is also reasonable to say that the dendritic layer enhancing effect, is limited until 3 mg cm^{-2} of D-Gold material deposited. Therefore, the red curve and the blue one in Fig. 6c almost overlap without highlighting other significant differences. On the contrary, there are relevant differences regarding the gray curve with 0.88 mg cm^{-2} compared to the red and blue ones in terms of capacitance performance.

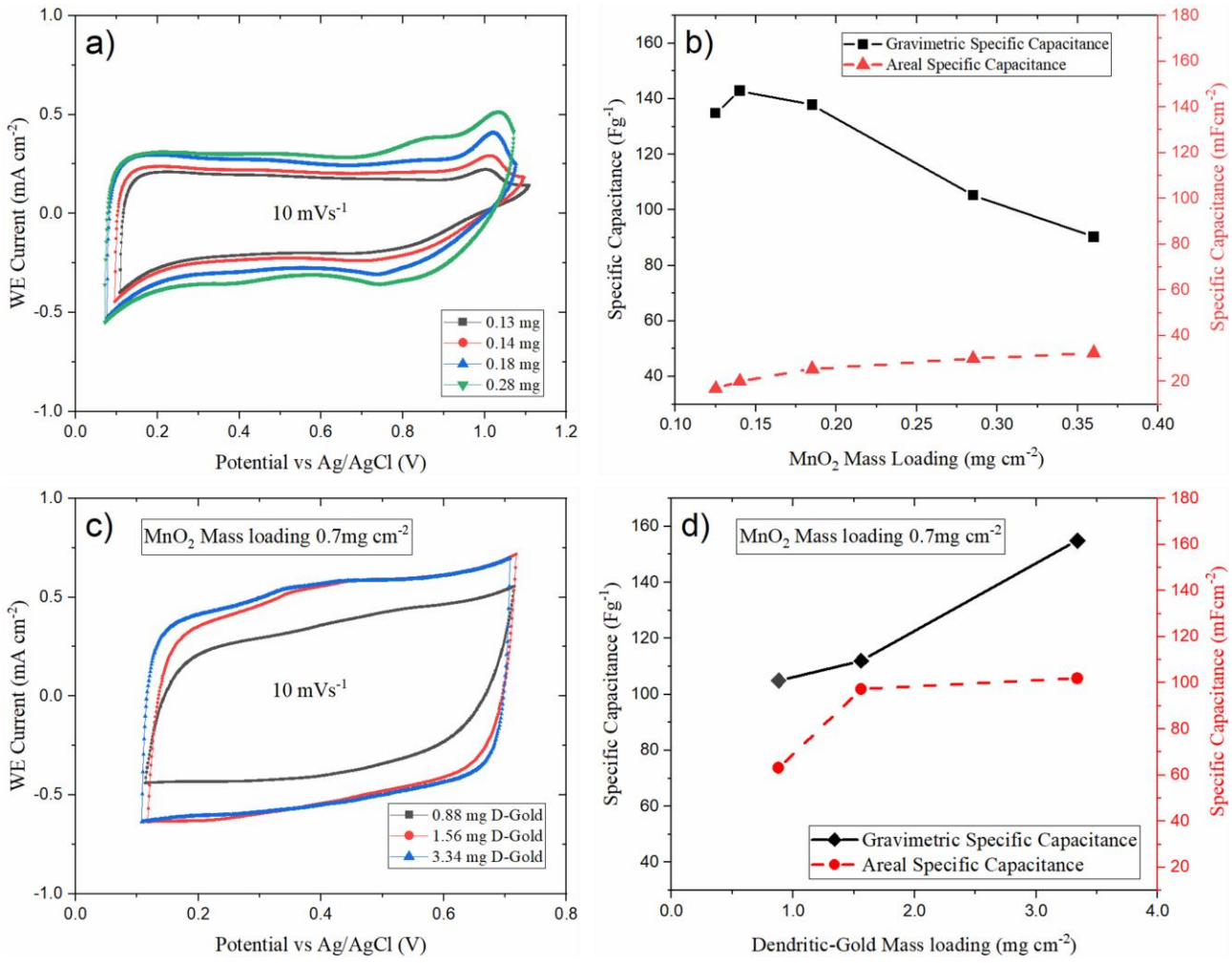

Fig. 6 (a) CV curves of MnO_2 loaded on to flat gold film, with differet MnO_2 mass loading, at a scan rate of 10 mV s^{-1}. (b) Gravimentric and areal capacitance perfomance in function of MnO_2 mass loading. (c) CV curves of MnO_2 deposited on D-Gold Current collector, varyng mass laoding of D-Gold, at a scan rate of 10 mVs^{-1}(d) Gravimentric and areal capacitance perfomance in function of D-Gold mass loading, with a fixed ammount of MnO_2 0.7mg cm^{-2}.

Fig. 6d shows the gravimetric capacitance and the specific capacitance per area unit calculated from eq. 5. It is possible to notice improved performances, tripled in terms of areal capacitance compared to the trendline in Fig. 6b, and to denote good stability of the gravimetric capacitance giving a specific value of about 100 $mFcm^{-2}$ for the MnO_2 electrode. Additional CVs were performed with D-Gold multilayered electrodes in two other neutral water-based electrolytes such as: K_2SO_4 and $MgSO_4$ (Fig. 7a, 7b, 7c). PEIS was performed before and after cycling voltametric measurements in order to

investigate possible changes or activation phenomena of the active material surface, as supported by Toupin et al. [69], cycling between 0 and 0.9 V can modify the oxidation state of the surface. Fig. 7a and 7b show different slopes of the PEIS curves. In each single curve, the slope raises after cycling. This difference is mainly justified by the intercalation, during the first cycles, of Na^+, K^+, Mg^{2+} cations in the bulk of MnO_2. Moreover, it is possible to note that better slope is reached by Na_2SO_4 electrolyte in regard to K_2SO_4 electrolyte in the lowest frequency region. Speaking of the negative electrode measurements, the electrochemical stability of the activated carbon electrode in the −1.1 V to 0 V vs Ag/AgCl voltage range was tested Na_2SO_4 1 M giving a specific capacitance of about 65 mF cm^{-2} (Fig. 7d). In this case it is useful to analyze and to make a comparison between PEIS of AC based electrode and the MnO_2 based electrode. The different morphological pore structures led to a different PEIS curve. The typical semi-circular pattern of carbon-based electrode is absent in MnO_2 based electrodes. This suggests a substantial difference in the porosity structure at the interface. PEIS of AC based electrode is more similar to line 4 in Fig. 7f describing an inner bulk porosity almost closed to the edge, while PEIS of MnO_2 based electrode is similar to lines 1-2 in Fig. 7f. where a well-open rectangular pore structure is portrayed.

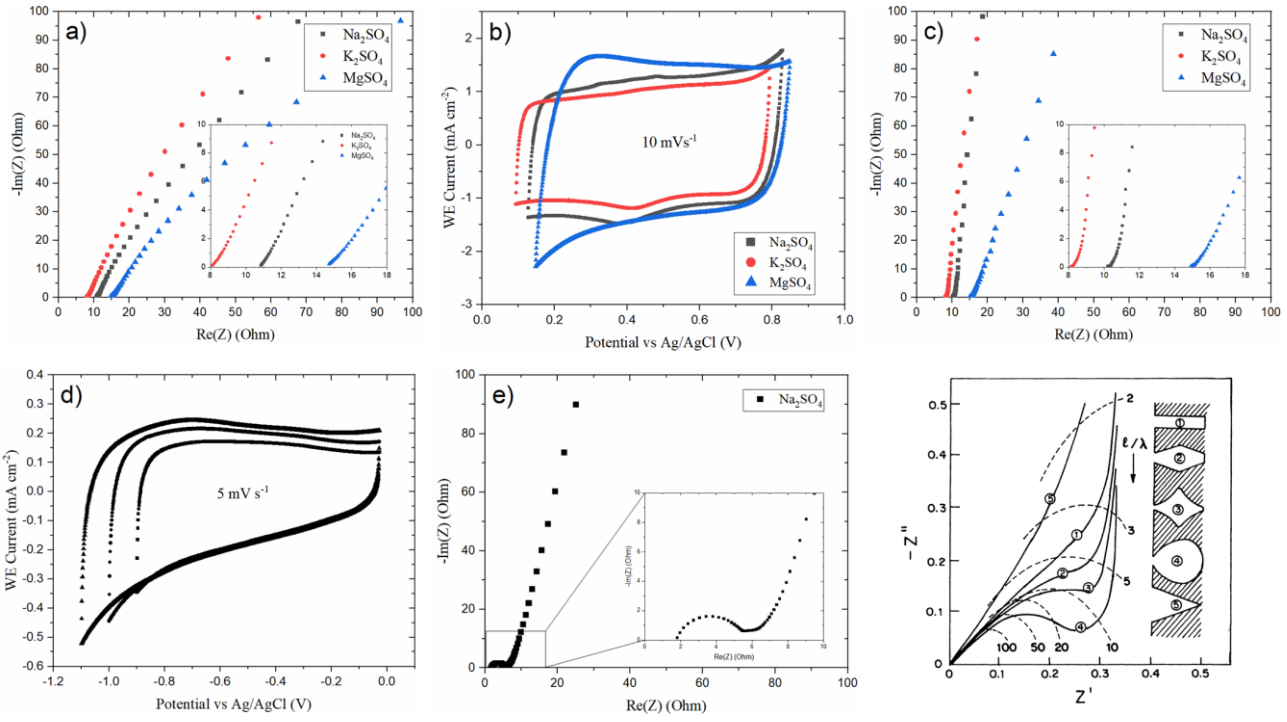

Fig. 7 (a) PEIS curve of MnO_2 electrode before cycling in differentt water based electrolyte. (b) CV curves for MnO_2 in differente water based electrolyte. At a scan rate of 10 mVs^{-1} (c) PEIS curve of MnO_2 electrode after cycling in differentt water based electrolyte. (d) CV curves for AC electrode at a scan rate of 5 mVs^{-1}. (e) PEIS curve of AC electrode after cycling. (f) Reprinted from [82], *Keiseret al. Abschätzung der porenstruktur poröser elektroden aus impedanzmessungen. Electrochim Acta 1976,21,539–543. Copyright 2022, with permission from Elsevier.*

3.3.3. Hybrid 2D Device Measurements

The hybrid device was built according to the procedure described in the experimental section. Electrodes were balanced in terms of charge, tuning the mass loading during the electroplating deposition techniques. The evolution of the cell voltage during charge/discharge cycle is shown in Fig. 8. PEIS was used to evaluate, mainly, the transport properties of the device; from the measurements resulted an equivalent series resistance of about 7 Ω. Capacitance changes with the scan rate, according to the different diffusion dynamics of the ions through the interface. At low scan rates, it is possible to observe the maximum charge accumulation process Fig. 8c, enabling full exploitation of pseudo-porosity. CCCD curves of the device denote a non perfectly linear behavior. This means that under the rate of 50 μAcm^{-2} self-discharge phenomena and electric losses occur. Non negligible is the possible presence of activated carbon particles along the separation, the particles could generate little resistive paths at the interface becoming terms for charge losses. Several future

analyses must be carried out to understand and limit the self-discharge effect. After an initial loss of 12 % observed during the first 100 cycles, the capacitance stabilized at 17 mF cm^{-2} cycling at 50 µmA cm^{-2}. The specific capacitance is calculated by the eq. 4. The capacitance retention plotted in Fig. 8d show stability for long cycling the performance of the device tested for over 1500 cycle at 500 µA cm^{-2} discharge current rate. However, the maximum energy density calculated from eq. 6 reached 5 µmWh cm^{-2} with a discharging time of 550 s. This time scale represents an appropriate time regime that can allow the use of MnO_2-based micro-supercapacitors for the initially proposed purposes, such as self-powered sensors, wearable electronics or many other applications where standard batteries suffer short time power requests. No visible gas evolution was noted during cycling. Device energy and power densities, evaluated by eq. 5 and eq. 6, are reported in Ragone plot Fig. 8e, and compared with electrochemical performances of planar devices present in last decades' literature, tested under similar conditions. Table 1 presents a comparison of the device tested in this work to the recent pseudocapacitive based micro-supercapacitor. As proposed in a recent review by Gao and Liu [70], for solid-state supercapacitors, the capacitance should be calculated considering the geometric area, since the active material weight is significantly lower if compared to the other constituents of the device. In this case the comparison was made considering only the areal capacitance, electrolyte and voltage windows of the various devices.

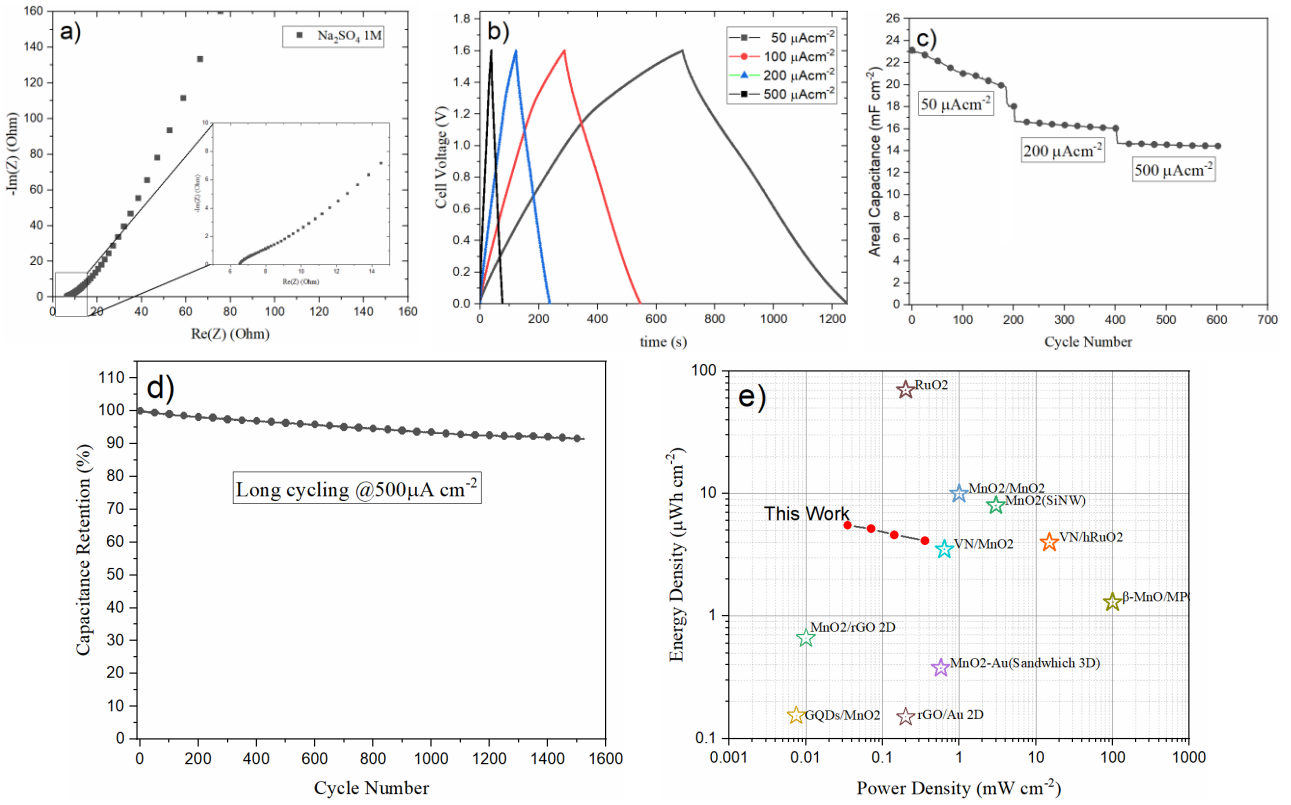

Fig. 6 (a) PEIS of the hybrid device. (b) CCCD curves of the hybrid device at a current density of 50–500 µA cm^{-2} (c) areal capacitance at different current rate (d) Capacitance retention of the devices at a current density of 500 µA cm^{-2} of 1600 cycles (e) Ragone plot of the presented work and previous pseudocapacitive micro-supercapacitors device presents in literature.

Table 1

Material	Capacitance mF/cm^{-2}	Electrolyte	Window V	C_{1000}/C_0	Ref.
MnO/AC (2D)	20 @50µAcm^{-2}	Na_2SO_4 1 M	1.6	90 %	**This Work**
MnO_2@SiNW (3D)	13 @10mVs^{-1}	LiClO4-PMPyrrBTA	2.2	90 %	[71] 10.1038/srep09771
GQDs/MnO 2	1.1 @15 µAcm^{-2}	Na_2SO_4 0.5 M	1	95 %	[72]

					10.1002/adfm.201203771
MnO_2/C/Al Nanowall Array	1000 @2 $mAcm^{-2}$	Na_2SO_4 1 M	1	90 %	[73] 10.1016/j.jpowsour.2015.09.029
MnO_2-Au (Sandwich-3D)	4.3 @50 μAcm^{-2}	Na_2SO_4 1 M	0.8	83 %	[74] 10.1002/smll.201503527
rGO/Au-FS	0.77@1 Vs^{-1}	PVA/H_2SO_4	1	71 %	[75] 10.1039/C5EE03637B
δ-MnO_2 (2D)	0.26@5.4 μAcm^{-2}	PEDOT	0.8	80 %	[76] 10.1016/j.nanoen.2018.05.002
VN/MnO_2 (2D)	16@1 mVs^{-1}	SiO2-LiTFSI gel	2.0	95 %	[77] 10.1016/j.ensm.2018.12.022
MnO_2/rGO	7.43@10 mVs^{-1}	PVA/H_3PO_4	0.8	100 %	[78] 10.1021/acsami.8b02660
RuO_2 (2D)	812@1 mVs^{-1}	PVA-doped-(SiWa)	0.9	95 %	[79] 10.1002/smll.201901224
β-MnO/MPG	6.5@1 Vs^{-1}	KOH	1.5	95 %	[80] 10.1109/LED.2021.3063474
VN/hRuO2	200@3.7 $mAcm^{-2}$	KOH 1 M	1.15	100 %	[27] 10.1016/j.ensm.2021.02.006
MnO_2/MnO_2 (ID)	50@10 mVs^{-1}	EMImTFSI+LiTFSI 0.5 M	1	--	[81] 10.1016/j.ensm.2022.05.041

4. Conclusion

This paper presented a complete preparation of a flexible planar 2D hybrid micro-supercapacitor. The combination of two deposition techniques applied to the same substrate, led to an important enhancement of the performance of the electrodes. We presented a hybrid capacitor with a negative AC composite electrode and a positive MnO_2 composite electrode, working in a neutral aqueous electrolyte. The processes for active material loading can be considered fully green, because only zero-impact materials using a water-based solution were involved during the process.

Furthermore, the materials involved are easily available in nature and this facilitates their supply. These are major strength points of this approach because they will ease the transition to sustainable large-scale production. The plating solution of Manganese on dendritic gold (D-gold) for the electrodes fabrication were tested and characterized by a mass loading curve. Physical analyses were performed to understand the morphology and quality of the electrode surface. A predominant presence of α-Mn_2O_3 phase (Bibyxite) was observed. Electrochemical analyses were successfully performed on the D-gold electrode denoting its great areal boost effect. We obtained a roughness factor of about 22 by adding a dendritic gold layer between the current collector and the active material layer. This means an enhancement of the areal factor of about 400 %. We observed that the electrode with the D-Gold layer can modify the behavior of the surface after cycling, modifying the slope of the PEIS curve. The final experimental results demonstrate a device with a large voltage window of 1.6 V in a water-based electrolyte, an areal capacitance of 20 mF cm^{-2}, a lifetime over 1500 cycle and a stable capacitance retention, over 90 %. This work aimed to simplify the procedures inherent to microfabrication, which is a necessary step to bring this technology to the level of a large scale production. The original approach proposed in this paper involves eco-friendly processes and low impact active material. Future research should further develop the integration of this technology with harvester batteries, and sensors in the IoT scenario.

5. Bibliography

[1] Bedi G, Venayagamoorthy GK, Singh R, Brooks RR, Wang K-C. Review of Internet of Things (IoT) in Electric Power and Energy Systems. IEEE Internet Things J 2018;5:847–70. https://doi.org/10.1109/JIOT.2018.2802704.

[2] Ai S, Chakravorty A, Rong C. Household Power Demand Prediction Using Evolutionary Ensemble Neural Network Pool with Multiple Network Structures. Sensors 2019;19:721. https://doi.org/10.3390/s19030721.

[3] d'Angelis O, di Biase L, Vollero L, Merone M. IoT architecture for continuous long term monitoring: Parkinson's Disease case study. Internet of Things 2022;20:100614. https://doi.org/10.1016/j.iot.2022.100614.
[4] Helal AA, Villaça RS, Santos CAS, Colistete R. An integrated solution of software and hardware for environmental monitoring. Internet of Things 2022;19:100518. https://doi.org/10.1016/j.iot.2022.100518.
[5] Sinnapolu G, Alawneh S. Intelligent wearable heart rate sensor implementation for in-vehicle infotainment and assistance. Internet of Things 2020;12:100277. https://doi.org/10.1016/j.iot.2020.100277.
[6] Hyysalo J, Dasanayake S, Hannu J, Schuss C, Rajanen M, Leppänen T, et al. Smart mask – Wearable IoT solution for improved protection and personal health. Internet of Things 2022;18:100511. https://doi.org/10.1016/j.iot.2022.100511.
[7] Sinnapolu G, Alawneh S. Integrating wearables with cloud-based communication for health monitoring and emergency assistance. Internet of Things 2018;1–2:40–54. https://doi.org/10.1016/j.iot.2018.08.004.
[8] Zaccagnini P, Ballin C, Fontana M, Parmeggiani M, Bianco S, Stassi S, et al. Laser- Induced Graphenization of PDMS as Flexible Electrode for Microsupercapacitors. Adv Mater Interfaces 2021;8:2101046. https://doi.org/10.1002/admi.202101046.
[9] Yin L, Wang J. Wearable Energy Systems: What are the Limits and Limitations? Natl Sci Rev 2022. https://doi.org/10.1093/nsr/nwac060.
[10] Oudenhoven JFM, Baggetto Loïc, Notten PHL. All-Solid-State Lithium-Ion Microbatteries: A Review of Various Three-Dimensional Concepts. Adv Energy Mater 2011;1:10–33. https://doi.org/10.1002/aenm.201000002.
[11] Sugiawati VA, Vacandio F, Yitzhack N, Ein-Eli Y, Djenizian T. Direct Pre-lithiation of Electropolymerized Carbon Nanotubes for Enhanced Cycling Performance of Flexible Li-Ion Micro-Batteries. Polymers (Basel) 2020;12:406. https://doi.org/10.3390/polym12020406.
[12] Toor A, Wen A, Maksimovic F, Gaikwad AM, Pister KSJ, Arias AC. Stencil-printed Lithium-ion micro batteries for IoT applications. Nano Energy 2021;82:105666. https://doi.org/10.1016/j.nanoen.2020.105666.
[13] Conway BE. Electrochemical Capacitors Based on Pseudocapacitance. Electrochemical Supercapacitors, Boston, MA: Springer US; 1999, p. 221–57. https://doi.org/10.1007/978-1-4757-3058-6_10.
[14] Guillemin T, Douard C, Robert K, Asbani B, Lethien C, Brousse T, et al. Solid-state 3D micro-supercapacitors based on ionogel electrolyte: Influence of adding lithium and sodium salts to the ionic liquid. Energy Storage Mater 2022;50:606–17. https://doi.org/10.1016/j.ensm.2022.05.041.
[15] Pech D, Brunet M, Durou H, Huang P, Mochalin V, Gogotsi Y, et al. Ultrahigh-power micrometre-sized supercapacitors based on onion-like carbon. Nat Nanotechnol 2010;5:651–4. https://doi.org/10.1038/nnano.2010.162.
[16] Tian J, Yu L, Xue R, Zhuang S, Shan Y. Global low-carbon energy transition in the post-COVID-19 era. Appl Energy 2022;307:118205. https://doi.org/10.1016/j.apenergy.2021.118205.
[17] Söderholm P. The green economy transition: the challenges of technological change for sustainability. Sustainable Earth 2020;3:6. https://doi.org/10.1186/s42055-020-00029-y.
[18] TRASATTI S. Electrochemistry and environment: The role of electrocatalysis*1. Int J Hydrogen Energy 1995;20:835–44. https://doi.org/10.1016/0360-3199(95)00014-5.
[19] Rafique A, Zubair U, Serrapede M, Fontana M, Bianco S, Rivolo P, et al. Binder Free and Flexible Asymmetric Supercapacitor Exploiting Mn3O4 and MoS2 Nanoflakes on Carbon Fibers. Nanomaterials 2020;10:1084. https://doi.org/10.3390/nano10061084.
[20] Hess LH, Wittscher L, Balducci A. The impact of carbonate solvents on the self-discharge, thermal stability and performance retention of high voltage electrochemical double layer

capacitors. Physical Chemistry Chemical Physics 2019;21:9089–97. https://doi.org/10.1039/C9CP00483A.
[21] Hess LH, Balducci A. 1,2-butylene carbonate as solvent for EDLCs. Electrochim Acta 2018;281:437–44. https://doi.org/10.1016/j.electacta.2018.05.168.
[22] Kang Q, Zhao J, Li X, Zhu G, Feng X, Ma Y, et al. A single wire as all-inclusive fully functional supercapacitor. Nano Energy 2017;32:201–8. https://doi.org/10.1016/j.nanoen.2016.12.020.
[23] Scalia A, Varzi A, Moretti A, Ruschhaupt P, Lamberti A, Tresso E, et al. Electrolytes based on N-Butyl-N-Methyl-Pyrrolidinium 4,5-Dicyano-2-(Trifluoromethyl) Imidazole for High Voltage Electrochemical Double Layer Capacitors. ChemElectroChem 2019;6:552–7. https://doi.org/10.1002/celc.201801172.
[24] Krause A, Kossyrev P, Oljaca M, Passerini S, Winter M, Balducci A. Electrochemical double layer capacitor and lithium-ion capacitor based on carbon black. J Power Sources 2011;196:8836–42. https://doi.org/10.1016/j.jpowsour.2011.06.019.
[25] Scalia A, Zaccagnini P, Armandi M, Latini G, Versaci D, Lanzio V, et al. Tragacanth Gum as Green Binder for Sustainable Water- Processable Electrochemical Capacitor. ChemSusChem 2021;14:356–62. https://doi.org/10.1002/cssc.202001754.
[26] Asbani B, Robert K, Roussel P, Brousse T, Lethien C. Asymmetric micro-supercapacitors based on electrodeposited Ruo2 and sputtered VN films. Energy Storage Mater 2021;37:207–14. https://doi.org/10.1016/j.ensm.2021.02.006.
[27] Asbani B, Robert K, Roussel P, Brousse T, Lethien C. Asymmetric micro-supercapacitors based on electrodeposited Ruo2 and sputtered VN films. Energy Storage Mater 2021;37:207–14. https://doi.org/10.1016/j.ensm.2021.02.006.
[28] Zhang SW, Chen GZ. Manganese oxide based materials for supercapacitors. Energy Materials 2008;3:186–200. https://doi.org/10.1179/174892409X427940.
[29] Paleo AJ, Staiti P, Rocha AM, Squadrito G, Lufrano F. Lifetime assessment of solid-state hybrid supercapacitors based on cotton fabric electrodes. J Power Sources 2019;434:226735. https://doi.org/10.1016/j.jpowsour.2019.226735.
[30] Serrapede M, Rafique A, Fontana M, Zine A, Rivolo P, Bianco S, et al. Fiber-shaped asymmetric supercapacitor exploiting rGO/Fe2O3 aerogel and electrodeposited MnOx nanosheets on carbon fibers. Carbon N Y 2019;144:91–100. https://doi.org/10.1016/j.carbon.2018.12.002.
[31] Rafique A, Massa A, Fontana M, Bianco S, Chiodoni A, Pirri CF, et al. Highly Uniform Anodically Deposited Film of MnO_2 Nanoflakes on Carbon Fibers for Flexible and Wearable Fiber-Shaped Supercapacitors. ACS Appl Mater Interfaces 2017;9:28386–93. https://doi.org/10.1021/acsami.7b06311.
[32] Nam K-W, Lee C-W, Yang X-Q, Cho BW, Yoon W-S, Kim K-B. Electrodeposited manganese oxides on three-dimensional carbon nanotube substrate: Supercapacitive behaviour in aqueous and organic electrolytes. J Power Sources 2009;188:323–31. https://doi.org/10.1016/j.jpowsour.2008.11.133.
[33] Boccaccini AR, Cho J, Roether JA, Thomas BJC, Jane Minay E, Shaffer MSP. Electrophoretic deposition of carbon nanotubes. Carbon N Y 2006;44:3149–60. https://doi.org/10.1016/j.carbon.2006.06.021.
[34] Atiq Ur Rehman M, Chen Q, Braem A, Shaffer MSP, Boccaccini AR. Electrophoretic deposition of carbon nanotubes: recent progress and remaining challenges. International Materials Reviews 2021;66:533–62. https://doi.org/10.1080/09506608.2020.1831299.
[35] Huq MM, Hsieh C-T, Ho C-Y. Preparation of carbon nanotube-activated carbon hybrid electrodes by electrophoretic deposition for supercapacitor applications. Diam Relat Mater 2016;62:58–64. https://doi.org/10.1016/j.diamond.2015.12.014.

[36] Kim T, Yi S-H, Chun S-E. Electrophoretic deposition of a supercapacitor electrode of activated carbon onto an indium-tin-oxide substrate using ethyl cellulose as a binder. J Mater Sci Technol 2020;58:188–96. https://doi.org/10.1016/j.jmst.2020.03.072.
[37] Pech D, Brunet M, Durou H, Huang P, Mochalin V, Gogotsi Y, et al. Ultrahigh-power micrometre-sized supercapacitors based on onion-like carbon. Nat Nanotechnol 2010;5:651–4. https://doi.org/10.1038/nnano.2010.162.
[38] Yu R, Wang J, Han M, Zhang M, Zeng P, Dang W, et al. Overcurrent Electrodeposition of Fractal Plasmonic Black Gold with Broad-Band Absorption Properties for Excitation-Immune SERS. ACS Omega 2020;5:8293–8. https://doi.org/10.1021/acsomega.0c00698.
[39] Massa A, Hernández S, Lamberti A, Galletti C, Russo N, Fino D. Electro-oxidation of phenol over electrodeposited MnOx nanostructures and the role of a TiO2 nanotubes interlayer. Appl Catal B 2017;203:270–81. https://doi.org/10.1016/j.apcatb.2016.10.025.
[40] Shen K, Ding J, Yang S. 3D Printing Quasi-Solid-State Asymmetric Micro-Supercapacitors with Ultrahigh Areal Energy Density. Adv Energy Mater 2018;8:1800408. https://doi.org/10.1002/aenm.201800408.
[41] Li L, Zhang J, Peng Z, Li Y, Gao C, Ji Y, et al. High-Performance Pseudocapacitive Microsupercapacitors from Laser-Induced Graphene. Advanced Materials 2016;28:838–45. https://doi.org/10.1002/adma.201503333.
[42] Hashmi SA, Latham RJ, Linford RG, Schlindwein WS. Conducting polymer-based electrochemical redox supercapacitors using proton and lithium ion conducting polymer electrolytes. Polym Int 1998;47:28–33. https://doi.org/10.1002/(SICI)1097-0126(199809)47:1<28::AID-PI3>3.0.CO;2-C.
[43] Ghosh K, Pumera M. MXene and MoS_{3-x} Coated 3D- Printed Hybrid Electrode for Solid-State Asymmetric Supercapacitor. Small Methods 2021;5:2100451. https://doi.org/10.1002/smtd.202100451.
[44] Sesen FE. Practical reduction of manganese oxide. Journal of Chemical Technology and Applications 2017;01. https://doi.org/10.35841/chemical-technology.1.1.26-27.
[45] Sesen FE. Practical reduction of manganese oxide. Journal of Chemical Technology and Applications 2017;01. https://doi.org/10.35841/chemical-technology.1.1.26-27.
[46] Hong MS, Lee SH, Kim SW. Use of KCl Aqueous Electrolyte for 2 V Manganese Oxide/Activated Carbon Hybrid Capacitor. Electrochemical and Solid-State Letters 2002;5:A227. https://doi.org/10.1149/1.1506463.
[47] Toupin M, Brousse T, Bélanger D. Influence of Microstucture on the Charge Storage Properties of Chemically Synthesized Manganese Dioxide. Chemistry of Materials 2002;14:3946–52. https://doi.org/10.1021/cm020408q.
[48] Wojdyr M. *Fityk* : a general-purpose peak fitting program. J Appl Crystallogr 2010;43:1126–8. https://doi.org/10.1107/S0021889810030499.
[49] van der PAUW LJ. A METHOD OF MEASURING SPECIFIC RESISTIVITY AND HALL EFFECT OF DISCS OF ARBITRARY SHAPE. Semiconductor Devices: Pioneering Papers, WORLD SCIENTIFIC; 1991, p. 174–82. https://doi.org/10.1142/9789814503464_0017.
[50] Biesinger MC, Payne BP, Grosvenor AP, Lau LWM, Gerson AR, Smart RStC. Resolving surface chemical states in XPS analysis of first row transition metals, oxides and hydroxides: Cr, Mn, Fe, Co and Ni. Appl Surf Sci 2011;257:2717–30. https://doi.org/10.1016/j.apsusc.2010.10.051.
[51] Chigane M, Ishikawa M. Manganese Oxide Thin Film Preparation by Potentiostatic Electrolyses and Electrochromism. J Electrochem Soc 2000;147:2246. https://doi.org/10.1149/1.1393515.
[52] Galakhov VR, Demeter M, Bartkowski S, Neumann M, Ovechkina NA, Kurmaev EZ, et al. Mn <math display="inline"> <mn>3</mn> <mi>s</mi> </math> exchange splitting in mixed-valence manganites. Phys Rev B 2002;65:113102. https://doi.org/10.1103/PhysRevB.65.113102.

[53] Di Castro V, Polzonetti G. XPS study of MnO oxidation. J Electron Spectros Relat Phenomena 1989;48:117–23. https://doi.org/10.1016/0368-2048(89)80009-X.
[54] Sun M, Lan B, Lin T, Cheng G, Ye F, Yu L, et al. Controlled synthesis of nanostructured manganese oxide: crystalline evolution and catalytic activities. CrystEngComm 2013;15:7010. https://doi.org/10.1039/c3ce40603b.
[55] Xin Y, Cao H, Liu C, Chen J, Liu P, Lu Y, et al. A systematic spectroscopic study of laboratory synthesized manganese oxides relevant to Mars. Journal of Raman Spectroscopy 2022;53:340–55. https://doi.org/10.1002/jrs.6231.
[56] Chen ZW, Lai JKL, Shek CH. Influence of grain size on the vibrational properties in Mn2O3 nanocrystals. J Non Cryst Solids 2006;352:3285–9. https://doi.org/10.1016/j.jnoncrysol.2006.04.011.
[57] Karuppaiah M, Sakthivel P, Asaithambi S, Murugan R, babu GA, Yuvakkumar R, et al. Solvent dependent morphological modification of micro-nano assembled Mn2O3/NiO composites for high performance supercapacitor applications. Ceram Int 2019;45:4298–307. https://doi.org/10.1016/j.ceramint.2018.11.104.
[58] Rahaman H, Laha RM, Maiti DK, Ghosh SK. Fabrication of Mn_2O_3 nanorods: an efficient catalyst for selective transformation of alcohols to aldehydes. RSC Adv 2015;5:33923–9. https://doi.org/10.1039/C5RA02504D.
[59] Garten LM, Selvarasu P, Perkins J, Ginley D, Zakutayev A. Phase formation of manganese oxide thin films using pulsed laser deposition. Mater Adv 2021;2:303–9. https://doi.org/10.1039/D0MA00417K.
[60] Ramírez A, Hillebrand P, Stellmach D, May MM, Bogdanoff P, Fiechter S. Evaluation of MnO_x, Mn_2O_3, and Mn_3O_4 Electrodeposited Films for the Oxygen Evolution Reaction of Water. The Journal of Physical Chemistry C 2014;118:14073–81. https://doi.org/10.1021/jp500939d.
[61] Javed Q, Feng-Ping W, Rafique MY, Toufiq AM, Iqbal MZ. Canted antiferromagnetic and optical properties of nanostructures of Mn_2O_3 prepared by hydrothermal synthesis. Chinese Physics B 2012;21:117311. https://doi.org/10.1088/1674-1056/21/11/117311.
[62] Post JE. Manganese oxide minerals: Crystal structures and economic and environmental significance. Proceedings of the National Academy of Sciences 1999;96:3447–54. https://doi.org/10.1073/pnas.96.7.3447.
[63] Ghosh SK. Diversity in the Family of Manganese Oxides at the Nanoscale: From Fundamentals to Applications. ACS Omega 2020;5:25493–504. https://doi.org/10.1021/acsomega.0c03455.
[64] Jarosch D. Crystal structure refinement and reflectance measurements of hausmannite, Mn3O4. Mineral Petrol 1987;37:15–23. https://doi.org/10.1007/BF01163155.
[65] Chen W, Wang N, Liu L, Cui Y, Cao X, Chen Q, et al. Facile synthesis of manganite nanowires: phase transitions and their electrocatalysis performance. Nanotechnology 2009;20:445601. https://doi.org/10.1088/0957-4484/20/44/445601.
[66] Song M-K, Cheng S, Chen H, Qin W, Nam K-W, Xu S, et al. Anomalous Pseudocapacitive Behavior of a Nanostructured, Mixed-Valent Manganese Oxide Film for Electrical Energy Storage. Nano Lett 2012;12:3483–90. https://doi.org/10.1021/nl300984y.
[67] Rand DAJ, Woods R. The nature of adsorbed oxygen on rhodium, palladium and gold electrodes. J Electroanal Chem Interfacial Electrochem 1971;31:29–38. https://doi.org/10.1016/S0022-0728(71)80039-6.
[68] Ferris A, Bourrier D, Garbarino S, Guay D, Pech D. 3D Interdigitated Microsupercapacitors with Record Areal Cell Capacitance. Small 2019;15:1901224. https://doi.org/10.1002/smll.201901224.
[69] Toupin M, Brousse T, Bélanger D. Charge Storage Mechanism of MnO_2 Electrode Used in Aqueous Electrochemical Capacitor. Chemistry of Materials 2004;16:3184–90. https://doi.org/10.1021/cm049649j.

[70] Liu N, Gao Y. Recent Progress in Micro-Supercapacitors with In-Plane Interdigital Electrode Architecture. Small 2017;13:1701989. https://doi.org/10.1002/smll.201701989.
[71] Dubal DP, Aradilla D, Bidan G, Gentile P, Schubert TJS, Wimberg J, et al. 3D hierarchical assembly of ultrathin MnO2 nanoflakes on silicon nanowires for high performance micro-supercapacitors in Li- doped ionic liquid. Sci Rep 2015;5:9771. https://doi.org/10.1038/srep09771.
[72] Liu W-W, Feng Y-Q, Yan X-B, Chen J-T, Xue Q-J. Superior Micro-Supercapacitors Based on Graphene Quantum Dots. Adv Funct Mater 2013;23:4111–22. https://doi.org/10.1002/adfm.201203771.
[73] He S, Zhang R, Zhang C, Liu M, Gao X, Ju J, et al. Al/C/MnO2 sandwich nanowalls with highly porous surface for electrochemical energy storage. J Power Sources 2015;299:408–16. https://doi.org/10.1016/j.jpowsour.2015.09.029.
[74] Hu H, Pei Z, Fan H, Ye C. 3D Interdigital Au/MnO_2/Au Stacked Hybrid Electrodes for On-Chip Microsupercapacitors. Small 2016;12:3059–69. https://doi.org/10.1002/smll.201503527.
[75] Li R-Z, Peng R, Kihm KD, Bai S, Bridges D, Tumuluri U, et al. High-rate in-plane micro-supercapacitors scribed onto photo paper using in situ femtolaser-reduced graphene oxide/Au nanoparticle microelectrodes. Energy Environ Sci 2016;9:1458–67. https://doi.org/10.1039/C5EE03637B.
[76] Wang Y, Zhang Y-Z, Dubbink D, ten Elshof JE. Inkjet printing of δ-MnO2 nanosheets for flexible solid-state micro-supercapacitor. Nano Energy 2018;49:481–8. https://doi.org/10.1016/j.nanoen.2018.05.002.
[77] Qin J, Wang S, Zhou F, Das P, Zheng S, Sun C, et al. 2D mesoporous MnO2 nanosheets for high-energy asymmetric micro-supercapacitors in water-in-salt gel electrolyte. Energy Storage Mater 2019;18:397–404. https://doi.org/10.1016/j.ensm.2018.12.022.
[78] Boruah BD, Maji A, Misra A. Flexible Array of Microsupercapacitor for Additive Energy Storage Performance Over a Large Area. ACS Appl Mater Interfaces 2018;10:15864–72. https://doi.org/10.1021/acsami.8b02660.
[79] Ferris A, Bourrier D, Garbarino S, Guay D, Pech D. 3D Interdigitated Microsupercapacitors with Record Areal Cell Capacitance. Small 2019;15:1901224. https://doi.org/10.1002/smll.201901224.
[80] Xia F, Xu S, Li S, Wang X. On-Chip High-Power Supply Unit: Micro Supercapacitor With Superb Capacitance Density and Fast Charge/Discharge Ability. IEEE Electron Device Letters 2021;42:625–8. https://doi.org/10.1109/LED.2021.3063474.
[81] Guillemin T, Douard C, Robert K, Asbani B, Lethien C, Brousse T, et al. Solid-state 3D micro-supercapacitors based on ionogel electrolyte: Influence of adding lithium and sodium salts to the ionic liquid. Energy Storage Mater 2022;50:606–17. https://doi.org/10.1016/j.ensm.2022.05.041.
[82] Keiser H, Beccu KD, Gutjahr MA. Abschätzung der porenstruktur poröser elektroden aus impedanzmessungen. Electrochim Acta 1976;21:539–43. https://doi.org/10.1016/0013-4686(76)85147-X.